Journal of Materials Chemistry A

PAPER

View Article Online
View Journal | View Issue

Cite this: J. Mater. Chem. A, 2018, 6, 2577

Tunable optical properties and stability of lead free all inorganic perovskites ($Cs_2SnI_xCl_{6-x}$)†

Weiguang Zhu,[a] Guoqing Xin,[a] Yiping Wang,[b] Xin Min,[c] Tiankai Yao,[a] Wenqian Xu,[d] Minghao Fang,[c] Sufei Shi,[ef] Jian Shi[b] and Jie Lian *[a]

Received 14th November 2017
Accepted 2nd January 2018

DOI: 10.1039/c7ta10040j

rsc.li/materials-a

Organic–inorganic hybrid lead-based perovskites experience significant environmental instability under ambient moist air and are not environmentally benign due to the usage of toxic Pb. Here, we report a new approach to synthesize lead-free all inorganic perovskites ($Cs_2SnI_xCl_{6-x}$) using hydriodic acid (HI) demonstrating greatly enhanced environmental stability and tunable optical properties by controlling the I^-/Cl^- ratios. Single phase perovskites can be achieved with a low iodine or chlorine content, and a phase separation occurs in the binary system with closer iodine and chlorine dopings. UV-vis diffuse reflectance and photoluminescence measurements reveal tunable band gaps of $Cs_2SnI_xCl_{6-x}$ perovskites from the UV to the infrared region. The mixed halide perovskite with a lower chloride content shows significantly higher photoluminescence intensity. The thermal stability of mixed halide all-inorganic perovskites is continuously improved as the Cl content increases. The synthesis of Sn-based perovskites with tunable optical properties and environmental stability represents one step further toward the realization of the stable lead-free all inorganic perovskites.

Introduction

Organic–inorganic perovskites have emerged as emerged as remarkable photovoltaic absorber materials recently, revolutionizing the design of emergent photovoltaics with a power conversion efficiency exceeding 20%.[1,2] However, the application of organic perovskites as absorber materials is limited by the heavy-metal toxic element lead (Pb) and environmental instability under ambient moist air, irradiation and heat exposure.[3,4] To overcome the challenging issues of Pb toxicity and moisture instability, it is critical to develop all inorganic lead-free perovskites, *e.g.*, by substitution of organic molecules with Cs^+ and lead with other non-toxic elements (*e.g.* Sn, Ge, Bi and Sb).[5–9] Sn-based $ASnI_3$ (A = $CH_3NH_3^+$ or Cs^+) perovskite solar cells without lead have been achieved.[5,10] However, these materials still exhibit significant instability along with phase transition due to the divalent Sn. Cs_2SnI_6 is a defect perovskite containing a stable and high oxidation state of Sn and has a direct bandgap (~1.3 eV). The lead-free perovskite Cs_2SnI_6 as a light absorber has been demonstrated for solar cell devices despite that the efficiency is relatively low.[11,12]

For $CH_3NH_3PbX_3$ (X = Cl, Br, or I)-based solar cells, the perovskite performance is strongly correlated to the nature of the halogen anions. Significant differences exist in the size and electronegativity among elements (Cl, Br and I), altering the optical and electronic properties and the stability of the corresponding compounds.[13] By mixing different halogens, an enhanced stability and tunable optoelectronic properties can be achieved.[14–16] Thus, a similar behavior is expected in the case of Cs_2SnI_6 perovskite. Recently, the incorporation of Br into Cs_2SnI_6 perovskite was obtained and the fabrication of $Cs_2SnI_{6-x}Br_x$ perovskite solar cell devices was demonstrated with an optimized power conversion efficiency (over 2%) and increased stability.[12]

In the current work, we develop a new approach to synthesize the iodide-based perovskite structure with a general formula of $Cs_2SnI_xCl_{6-x}$ which shows greatly enhanced environmental/thermal stability and tunable optical properties. The amount of iodide in the binary system can be controlled using hydriodic acid (HI) as the iodide source, in which iodide can be incorporated into the Cs_2SnCl_6 matrix by anion substitution. Single phase perovskites are obtained at either ends of iodide or chloride-enriched compositions. Interestingly, a unique phase

[a]Department of Mechanical, Aerospace and Nuclear Engineering, Rensselaer Polytechnic Institute, Troy, New York 12180, USA. E-mail: lianj@rpi.edu; Fax: +1 518-276-6025; Tel: +1 518-276-6081

[b]Department of Materials Science and Engineering, Rensselaer Polytechnic Institute, Troy, New York 12180, USA

[c]Beijing Key Laboratory of Materials Utilization of Nonmetallic Minerals and Solid Wastes, National Laboratory of Mineral Materials, School of Materials Science and Technology, China University of Geosciences (Beijing), Beijing 100083, PR China

[d]X-ray Science Division, Advanced Photon Source, Argonne National Laboratory, Lemont, Illinois 60439, USA

[e]Department of Chemical and Biological Engineering, Rensselaer Polytechnic Institute, Troy, New York 12180, USA

[f]Department of Electrical, Computer and Systems Engineering, Rensselaer Polytechnic Institute, Troy, New York 12180, USA

† Electronic supplementary information (ESI) available. See DOI: 10.1039/c7ta10040j

separation behavior occurs in the binary $Cs_2SnI_xCl_{6-x}$ system with co-existing two phases with either Cl- and I-enriched compositions at closer I/Cl dopings (Fig. 1). The band gap can be tuned monotonically from ~1.3 to ~4.6 eV as measured by UV-vis spectroscopy. Meanwhile, the high iodide doping with a low chloride content perovskite shows much higher photoluminescence intensity than that of pure Cs_2SnI_6, indicating an enhanced exciton lifetime. Our study can thus improve the knowledge on $Cs_2SnI_xCl_{6-x}$ perovskite phase behavior and could help in refining the material preparation strategy for the realization of better hybrid lead-free all inorganic perovskites.

Experimental section

Materials

All chemicals used are as-purchased without further purification. Cesium iodide (CsI, 99.9%), cesium chloride (CsCl, 99%), *n*-butyl acetate (99% min), and hydroiodic acid (HI, 55–58%) were purchased from Alfa Aesar. Tin(IV) chloride pentahydrate ($SnCl_4 \cdot 5H_2O$, 98%), tin powder (Sn, ≥99%) and iodine (I_2, ≥99.99%) were purchased from Sigma Aldrich.

Synthesis of $Cs_2SnI_xCl_{6-x}$

$Cs_2SnI_xCl_{6-x}$ samples were prepared by tuning the addition of hydroiodic acid to achieve different I^-/Cl^- ratios. Briefly, CsCl (1 mmol) was dissolved in 10 mL of methanol upon heating the solution to ~60 °C using a water bath under constant magnetic stirring. $SnCl_4 \cdot 5H_2O$ (0.5 mmol) was dissolved in a mixture of 5 mL *n*-butyl acetate and HI (0, 1, 2, 2.5, 3, and 4 mL). Then, the addition of the $SnCl_4$ mixture to CsCl solution led to the precipitation of iodide incorporated samples. Based on the amount of HI, the color of precipitated powders can be tuned continuously. Then the solids were washed with *n*-butly acetate twice *via* centrifuging and dried in an oven at 80 °C overnight under ambient conditions. Following a similar procedure, the synthesis of Cs_2SnI_6 was carried out by mixing stoichiometric amounts of CsI (1 mmol in 10 mL methanol) and SnI_4 (0.5 mmol dissolved in 5 mL *n*-butyl acetate and 2 mL HI) in a 2 : 1 molar ratio. SnI_4 was prepared by reaction of Sn and I_2 in warm dichloromethane (DCM) solution. 1.0 g of Sn powder and 2.5 g of I_2 were loaded into a 50 mL beaker along with addition of 10 mL DCM. Then the beaker was covered with a glass slide and heated gently on a hot plate to avoid DCM boiling. The solution was stirred for 30–40 minutes until there was no visible violet color. The warm solution was filtered into another 50 mL beaker to remove excess Sn powder and cooled in an ice bath. The bright orange crystals were collected by filtration and washed with 5 mL of cold DCM. The solid was dried in a vacuum oven overnight.

Characterization

Synchrotron powder X-ray diffraction (XRD) data were collected on the 17-BM beamline at the Advanced Photon Source, Argonne National Laboratory. The experiment was carried out by loading approximately 5 mg of powder sample in a Kapton tube of 1.1 mm diameter. The X-ray wavelength utilized for synchrotron X-ray diffraction is 0.39433 Å. X-ray diffraction patterns were analyzed using the Rietveld refinement functions implemented in GSAS II.[17,18] The crystal structures were illustrated using VESTA.[19] Lab XRD was also performed on the all-inorganic perovskites using a Panalytical X'pert Pro system (Westborough, MA, USA) with a copper target (K_α = 1.5406 Å). Morphology and energy-dispersive X-ray elemental analysis was carried out using a Carl Zeiss Supra 55 field emission scanning electron microscope (FESEM) with an Oxford energy-dispersive X-ray spectrometer (EDS). Thermogravimetric analysis (TGA) of $Cs_2SnI_{6-x}Cl_x$ was conducted using a TGA-Q50 system from TA Instruments.

UV-visible diffuse reflectance spectroscopy was performed on the powder samples of the mixed halide perovskite $Cs_2SnI_xCl_{6-x}$. The spectra were acquired using a Varian Cary 6000i UV-vis-NIR spectrometer with Praying Mantis diffuse

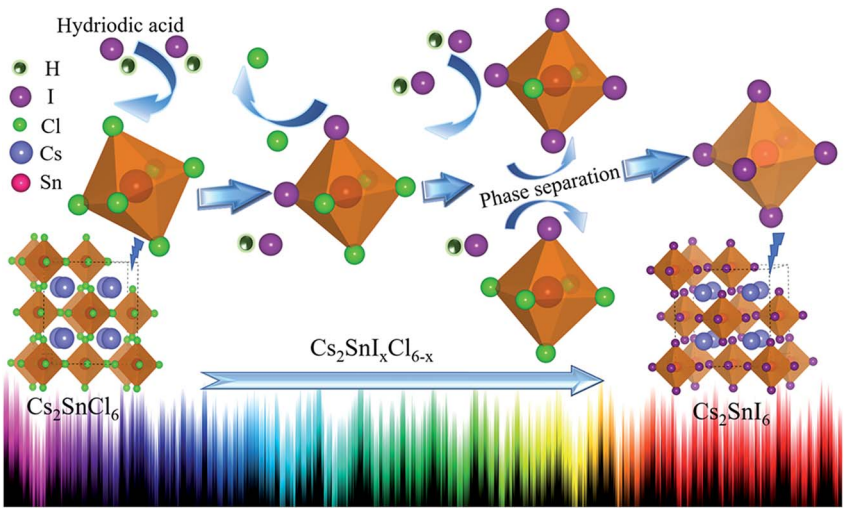

Fig. 1 Schematic synthesis of the mixed halide perovskite $Cs_2SnI_xCl_{6-x}$ using hydriodic acid, and the color scheme displays the tunable band gap with varying I^-/Cl^- ratios.

reflectance accessories from $\lambda = 350$ nm to 1200 nm at a scan rate of 300 nm min^{-1}. Photoluminescence (PL) measurements were carried out at room temperature using a customized PL system consisting of a PicoQuant 405 nm pulsed laser with 2 mW power, a Nikon Eclipse Ti–S inverted optical microscope, a Princeton Instruments SP-2358 spectrograph and a PicoQuant PDM single photo avalanche photodetector. Additional samples (labelled S6 and S7) were measured on another home-built system with a 532 nm CW laser and a Si photodetector. Time-resolved photoluminescence (TRPL) was performed using a tunable Ti:saphhire femtosecond-pulsed laser as the excitation light source to generate the excitation light at a wavelength of 475 nm with a repetition frequency of 80 MHz.

Results and discussion

We developed a new strategy to obtain lead-free all inorganic perovskites $Cs_2SnI_xCl_{6-x}$, and the compositions of the mixed halide perovskites were tuned using varying amounts of hydriodic acid solution as described in detail in the Experimental section. Without HI, it is difficult to obtain the mixed halide perovskite $Cs_2SnI_xCl_{6-x}$ series since iodide-based perovskites dissolve in organic solvents. Particularly, Cs_2SnI_6 has good solubility in organic solvents (*e.g.* ethanol, methanol, and DMF) and the color of the solution is close to that of SnI_4, indicating that it may decompose into SnI_4 and CsI in the solution, as shown in Fig. S1a.† The UV-vis absorption measurement shows that Cs_2SnI_6 solution has the same absorption edge of SnI_4, which confirms the decomposition of Cs_2SnI_6 (Fig. S2a†). In addition, the recrystallized powder after evaporating the solution at 60 °C consists of CsI and a small amount of Cs_2SnI_6 and CsI_3 (Fig. S2b†). Similarly, for high iodide doped samples, it dissolves in the organic solution. On the other hand, low iodide doped samples have much lower solubility, as shown in Fig. S1b.† Inspired by the previous findings of a stabilized tetragonal $MAPbI_3$ phase using hydriodic acid,[20] here we use hydriodic acid to stabilize the crystal structure of iodide doped compositions, which also acts as an iodide source. As shown in the optical images (Fig. 2a), the distinguished colors of the mixed halide perovskite indicate different amounts of I/Cl incorporation. The color of the samples from S1 to S7 changes progressively from white to completely black. SEM analysis indicates that the particle sizes of synthesized samples increase systematically upon increasing the I content in $Cs_2SnI_xCl_{6-x}$. Pure Cs_2SnI_6 has a crystallite size around 15 μm with octahedral shapes whereas pure Cs_2SnCl_6 has much smaller crystallites (~50 nm), as shown in Fig. 2b. Following this trend, the particle size of the the intermediate $Cs_2SnI_xCl_{6-x}$ compositions lie in between these two extremes. This morphology transformation suggests distinct rates of homogenous nucleation/precipitation and grain growth from solution. A similar trend was reported for $Cs_2SnI_{6-x}Br_x$ series by Lee *et al.*[12]

The EDS analysis (Table 1) further demonstrates that the composition can be tuned systematically from pure Cl (Cs_2SnCl_6) to nearly 100% I (Cs_2SnI_6) (see sample S1 to S7). The I content increases from 0% for S1 to 57.6% for S6, while the Cl content decreases from 64% for S1 to 9.1% for S6. For organic–inorganic hybrid perovskites $MAPbI_{3-x}Cl_x$, several reports

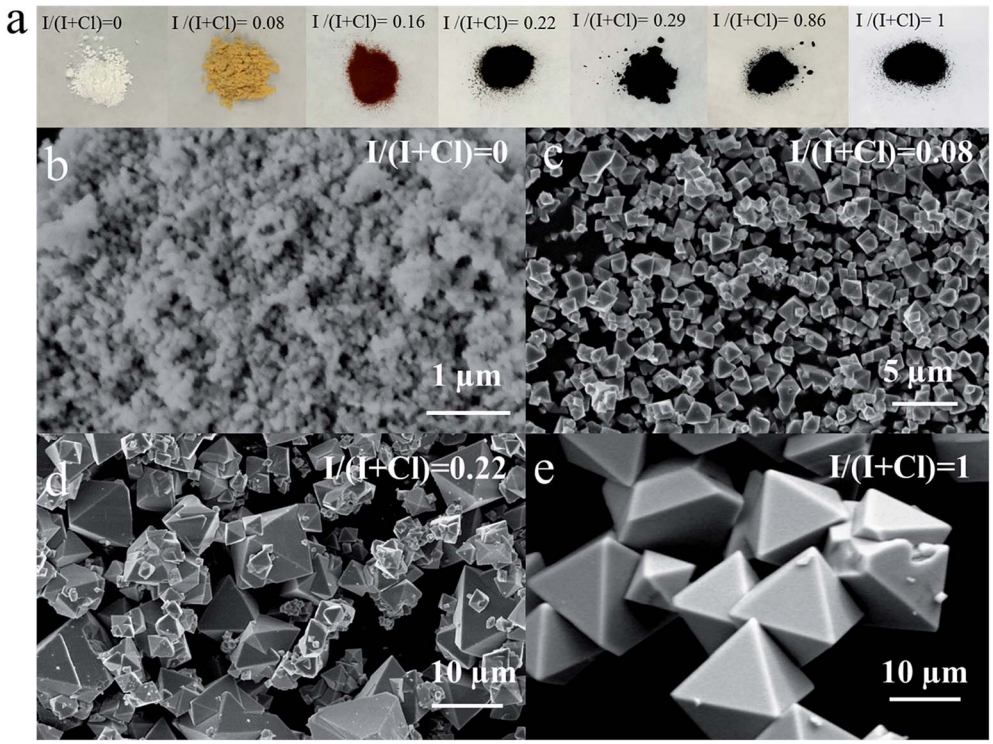

Fig. 2 (a) The optical images of the mixed halide perovskites $Cs_2SnI_xCl_{6-x}$ with various iodide contents; SEM images of (b) sample S1, (c) sample S2, (d) sample S4, and (e) sample S7. Note: sample S1 and S7 are pure Cs_2SnCl_6 and Cs_2SnI_6 powder, respectively.

Table 1 The atomic percentage of the 4 elements (Cs, Sn, Cl, and I) for samples S1 to S7, as measured by EDS spectroscopy

	S1	S2	S3	S4	S5	S6	S7
Cs	23.91	24.97	25.62	21.91	21.53	21.55	20.10
Sn	12.02	12.92	13.25	11.59	11.32	17.76	10.41
Cl	64.06	57.39	51.49	51.93	47.47	9.12	0
I	0	4.72	9.63	14.57	19.67	57.57	69.49
I/(I + Cl)	0	0.08	0.16	0.22	0.29	0.86	1

pointed out that chloride could hardly incorporate into the lattice and only a negligible amount of Cl can be detected if present, from residual precursors.[16,21–23] Fig. S3a† shows the SEM image of well-faceted perovskite crystals (Cs_2SnI_6). EDS mapping (Fig. S3b–d†) reveals the homogeneous presence of the constituent atoms of Cs, Sn, and I throughout the dimension of perovskite crystals. Furthermore, we analyzed sample S3. Fig. 3a shows a much smaller crystal size than Cs_2SnI_6, which is consistent with the above analysis. EDS mapping results (Fig. 3b–e) show a uniform distribution of the four elements (Cs, Sn, I and Cl), indicating a mixed halide crystal structure. It is worth noting that due to the limited resolution of EDS, the sample homogeneity was further demonstrated by using X-ray diffraction patterns in the later section. In addition, the I-rich region can be seen in some grains for higher iodide incorporation, which is related to phase separation behavior and will be discussed in the following section (see ESI Fig. S4†). For more compositions, the detailed EDS mapping results can be found in the ESI (Fig. S5 and S6†).

Fig. 4a shows the full-range synchrotron X-ray powder diffraction patterns of the mixed halide perovskite in the binary system of $Cs_2SnI_xCl_{6-x}$. The diffraction patterns for the entire series at room temperature present reflections consistent with the cubic ($Fm\bar{3}m$ space group) vacancy-ordered double perovskite. Rietveld analysis yields lattice parameters of 11.6517(2) Å and 10.3923(2) Å for the end members of Cs_2SnI_6 and Cs_2SnCl_6, respectively. A systematic peak shift in the patterns to lower diffraction angles is observed with increasing iodide concentration, indicating an expansion of the unit cell at greater iodide fractions. Fig. 4b shows the (311) and (222) peaks on a magnified scale. From samples S1 to S3, the peaks shift to lower 2θ degrees monotonically and the lattice parameters exhibit a linear relationship with the I content increase, as shown in Fig. 4c. According to Vegard's law, the variation of the lattice parameter in a solid solution follows a linear change with the composition in the absence of strong electronic effects.[14,24] From Rietveld refinements of the site occupancies, the compositions of sample S2 and S3 were determined as $Cs_2SnI_{0.43}Cl_{5.57}$ and $Cs_2SnI_{0.90}Cl_{5.10}$, respectively. Moreover, as the iodide concentration increases, an interesting phase behavior was observed in which $Cs_2SnI_xCl_{6-x}$ separates into two phases. For sample S4, every peak split into two close peaks, indicating two phases with a similar structure. The compositions of two phases for sample S4 are $Cs_2SnI_{1.3}Cl_{4.7}$ and $Cs_2SnI_{0.7}Cl_{5.3}$, respectively. It should be noted that besides the two similar compositions, sample S4 also contains a third phase ($Cs_2SnI_{5.21}Cl_{0.79}$) with the composition close to Cs_2SnI_6.

Further increasing the iodide concentration leads to a phase separation with Cl- and I-enriched phases (*i.e.* $Cs_2SnI_{0.44}Cl_{5.56}$ and $Cs_2SnI_{5.26}Cl_{0.74}$), as shown in the diffraction pattern of sample S5. We ascribe this phenomenon to the significant size difference between iodide (2.20 Å) and chloride anions (1.81 Å),[25] causing a large lattice distortion. While with a higher iodide concentration, it forms the single phase I-rich end, as sample S6 ($Cs_2SnI_{5.28}Cl_{0.72}$). Thus, it is worth pointing out that the $Cs_2SnI_3Cl_3$ perovskite could hardly be synthesized by the solution based method at low temperature. Our results suggest that the maximum iodide incorporation into the Cl-enriched single phase $Cs_2SnI_xCl_{6-x}$ is less than 1 and the chloride content is less than 1 in the I-enriched single phase Cs_2SnI_x-Cl_{6-x} system. The structural parameters and refinement statistics are compiled in Table S1.†

Because of significant differences in the crystal size and electronegativity among elements (Cl, Br and I), it is expected that the optical and electronic properties and the stability of the

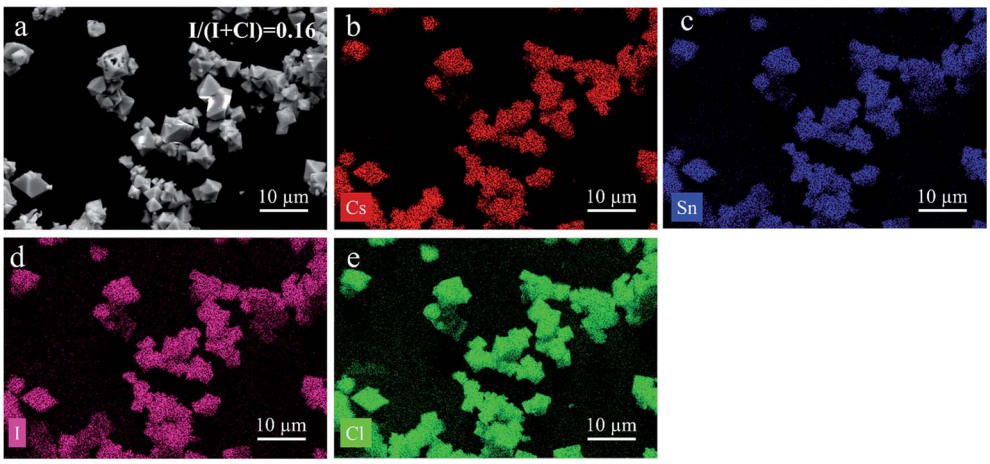

Fig. 3 A SEM image (a) of the sample S3 showing the morphology of the recrystallized particles and energy-dispersive X-ray mapping showing the elemental distributions of the Cs map (b), Sn map (c), I map (d), and Cl map (e).

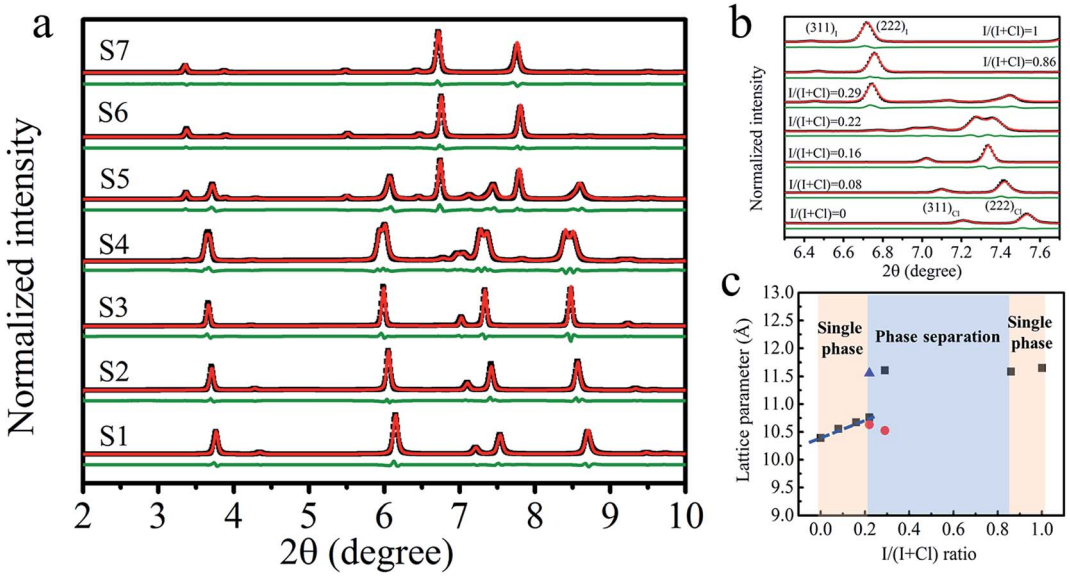

Fig. 4 (a) Synchrotron X-ray diffraction patterns and Rietveld refinements of the binary system $Cs_2SnI_xCl_{6-x}$ at room temperature (black squares represent the data, red lines represent the fitting curves, and the green lines are the differences); (b) (311) and (222) peaks in a close-up view showing systematic shifts to a lower angle with increasing iodide incorporation. The subscripts I and Cl represent the pure Cs_2SnI_6 and Cs_2SnCl_6, respectively; and (c) the refined lattice parameter as a function of iodide atomic concentration measured by EDS.

corresponding compounds can be altered as reported in the Pb^{2+} and Sn^{2+} systems.[14,26–28] The measured UV-vis spectra and PL of the mixed halide perovskite series $Cs_2SnI_xCl_{6-x}$ are shown in Fig. 5. The color of pure Cs_2SnCl_6 is white (Fig. 2a), suggesting that there is no absorption in the visible range, consistent with its band gap (E_g) ~4.6 eV. For Cs_2SnI_6 (Fig. 5a), the onset absorption is at the wavelength of 941 nm (1.32 eV), consistent with a previous report.[29] The substitution of chlorine with iodine atoms is expected to decrease the band gap of the mixed halide perovskite.[30] With increasing iodide content, the onset absorption band of $Cs_2SnI_xCl_{6-x}$ perovskites can be tuned from a 373 nm wavelength (3.32 eV) to a 900 nm wavelength

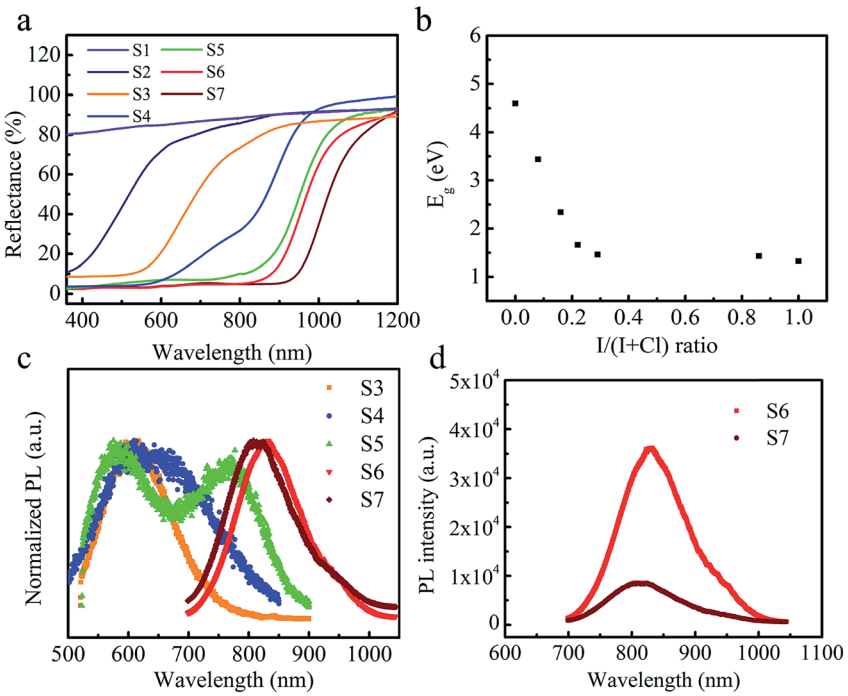

Fig. 5 (a)The UV-vis diffuse reflectance spectra of the binary series $Cs_2SnI_xCl_{6-x}$; (b) the measured band gap energy as a function of iodide atomic concentration. The E_g was estimated from the onset absorption band of UV-vis spectra; (c) PL analysis of various $Cs_2SnI_xCl_{6-x}$ compositions measured at room temperature; and (d) PL spectra of S6 ($Cs_2SnI_{5.28}Cl_{0.72}$) and S7 (Cs_2SnI_6).

(1.38 eV), close to that of Cs_2SnI_6. A systematic shift of the absorption edge to longer wavelengths with increasing I contents in $Cs_2SnI_xCl_{6-x}$ indicates that the band gap (E_g) can be tuned by using the composition of the solid solution, as shown in Fig. 5a. The E_g was estimated from the onset absorption band of the UV-vis spectra and is plotted in Fig. 5b with the variation of I contents in $Cs_2SnI_xCl_{6-x}$. It is seen that E_g decreases monotonically from 4.6 eV for S1 to 1.32 eV for S7.

A similar trend was observed from the PL characterization (Fig. 5c). For sample S4 and S5, it shows two distinguished peaks due to the phase separation. The detailed multiple peak fittings can be found in Fig. S7.† For sample S6 ($Cs_2SnI_{5.28}Cl_{0.72}$) and S7 (Cs_2SnI_6), close band gaps were observed due to the low chloride concentration. Interestingly, the PL intensity of $Cs_2SnI_{5.28}Cl_{0.72}$ is significantly higher than that of Cs_2SnI_6. The higher PL intensity of $Cs_2SnI_{5.28}Cl_{0.72}$ suggests increased quantum efficiency, which could be due to the combination of the exciton lifetime and the increased radiative recombination rate.[31,32] It is intriguing that such a slight change in the composition can lead to such a significant enhancement in the optical properties. The exact reason is still not clear and requires further investigation. The time-resolved photoluminescence (TRPL) was performed to analyze the carrier lifetime. As shown in Fig. S8,† the Cl-doped sample S6 ($Cs_2SnI_{5.28}Cl_{0.72}$) has a similar lifetime to Cs_2SnI_6 (sample S7). The PL decay curves are fitted with a biexponential function. The lifetime of Cs_2SnI_6 has a fast component of 0.06 ns and a slow component of 0.27 ns, similar to the results reported in the literature.[33] For $Cs_2SnI_{5.28}Cl_{0.72}$, the fast and slow components are 0.08 ns and 0.45 ns, respectively. Overall, it is fascinating that the band gap can be systematically tuned across a wide range upon iodide incorporation and this is of great interest to various applications from colorful solar cells, energy harvesting, tunable light emitting and sensing.

Due to the high oxidation state of Sn, Cs_2SnI_6 shows good stability without obvious decomposition under ambient conditions for over 2 months. After 4 months of storage in air, only a trace amount of CsI impurity appears in the original powder (Fig. S9a†). However, the synthesized all inorganic mixed halide perovskite ($Cs_2SnI_{5.28}Cl_{0.72}$) shows greatly improved environmental stability without degradation under ambient conditions for more than 5 months (see Fig. S9b†). For the optical properties, $Cs_2SnI_{5.28}Cl_{0.72}$ does not show significant difference after 5 months. However, an obvious blue shift of the absorption edge was observed for the sample Cs_2SnI_6 stored for over 5 months, as shown in Fig. S10.† To further test its environmental stability, thermogravimetric analysis (TGA) was performed on the all-inorganic mixed halide perovskite $Cs_2SnI_xCl_{6-x}$. As shown in Fig. 6, the thermal decomposition of Cs_2SnI_6 starts at ~300 °C (*i.e.*, the extrapolated onset temperature is $T_0 = 317$ °C, as shown in Fig. 6c), consistent with the result reported earlier.[34] After the decomposition of Cs_2SnI_6, the left-over powder is about 45% of the initial weight, indicating that the residual powder is CsI, which constitutes 45.3% of the atomic weight in Cs_2SnI_6. It is also confirmed by the XRD result tested on the residual powder (Fig. S11a†). With increasing chloride content, the decomposition temperature increases accordingly (Fig. 6a). As to Cs_2SnCl_6, the decomposition temperature is above 550 °C, which is much higher than that of Cs_2SnI_6 (Fig. 6d). The residual powders consist of CsCl and SnO_2, as shown in Fig. S11b.† Since the decomposed product $SnCl_4$ is very hygroscopic, the presence of SnO_2 could be ascribed to the

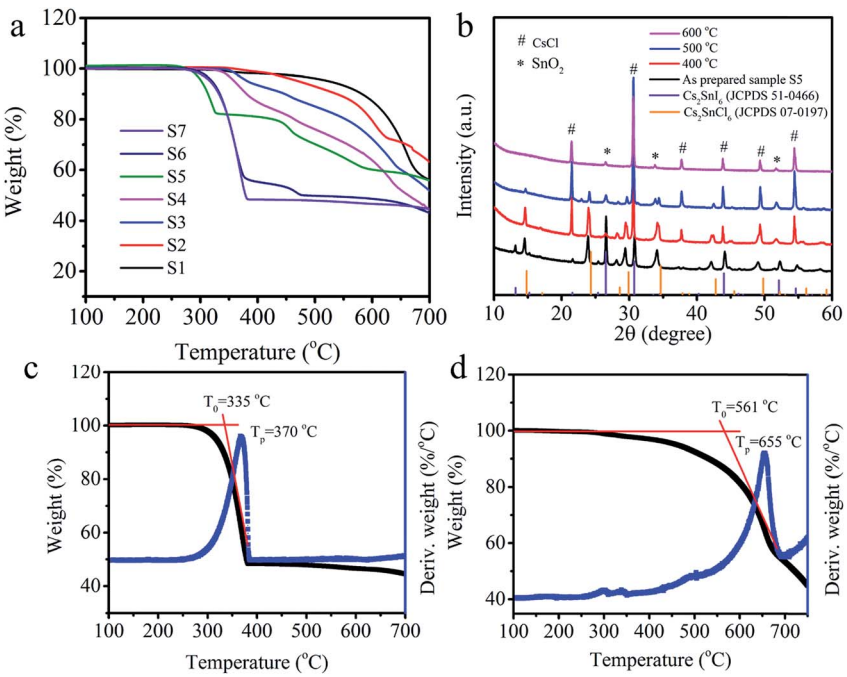

Fig. 6 (a) Thermogravimetric analysis (TGA) curves of the solid solution series $Cs_2SnI_xCl_{6-x}$. (b) XRD patterns of sample S5 ($Cs_2SnI_{0.44}Cl_{5.56}$ and $Cs_2SnI_{5.26}Cl_{0.74}$) after TGA tests at various temperatures, *i.e.* 400 °C, 500 °C, and 600 °C. The onset temperature and the first order derivative of TGA for (c) Cs_2SnI_6 and (d) Cs_2SnCl_6, respectively.

decomposition of the hydrated $SnCl_4$. The decomposition process of $Cs_2SnI_xCl_{6-x}$ can be separated into several stages with different decomposition temperatures. For sample S3 ($Cs_2SnI_{0.90}Cl_{5.10}$), it shows two different decomposition regions at 380 °C and 550 °C, respectively. This is because the iodide-doped sample decomposed in the first decomposition region, and a part of the decomposition products reacted with the residual powder sample forming the Cl-enriched phase. This contributes to the second decomposition regime with a decomposition temperature close to that of Cs_2SnCl_6. A similar phenomenon was observed from sample S4, which mainly contains two close iodide-doped phases. For sample S5, it is composed of two different phases, I-rich ($Cs_2SnI_{5.26}Cl_{0.74}$) and Cl-rich ($Cs_2SnI_{0.44}Cl_{5.56}$) phases. Hence it shows obviously two decomposition regions. We conducted TGA tests on sample S5 at various temperatures to investigate its decomposition mechanism, *i.e.* 400 °C, 500 °C, and 600 °C. Fig. 6b shows the XRD patterns of the products after TGA tests at different temperatures. As the sample was heated to 400 °C, the I-rich perovskite decomposed, and only the Cl-rich perovskite phase and CsCl were left. The Cl-rich perovskite phase suffered iodide loss and transformed to a phase that is closer to pure Cs_2SnCl_6. It is worth mentioning that there is no CsI detected, as expected for the decomposition product of the I-rich perovskite. It may be due to the formation of cesium polyiodide (such as CsI_3) under the decomposed iodide rich environment. This new phase has a low melting point (~210 °C)[35] and is evaporated during heating. For the 500 °C heated sample, the Cl-rich phase started to decompose at a temperature of ~430 °C and the observed decomposed product is CsCl. On further heating to 600 °C, it is fully decomposed and only decomposition products (CsCl and SnO_2) were observed, similar to Cs_2SnCl_6. For the decomposition mechanism of the $Cs_2SnI_xCl_{6-x}$ perovskite, further investigation is still needed.

Conclusions

A new approach was developed to synthesize the mixed halide lead free all inorganic perovskites $Cs_2SnI_xCl_{6-x}$ using HI solution to achieve various iodide/chloride incorporations. A single phase solid solution can be obtained at the both ends of Cl- or I-enriched compositions with maximum incorporation of iodine less than 1 or chloride content less than 1 in the binary system composition $Cs_2SnI_xCl_{6-x}$ or $Cs_2SnI_{6-x}Cl_x$, respectively. The optical absorption can be systematically tuned into a wide range from UV to infrared. Meanwhile, the mixed halide perovskite with a low chloride content can significantly enhance the optical properties with much higher PL intensity. The synthesized all inorganic mixed halide perovskites show greatly improved environmental stability without degradation under ambient conditions. The incorporation of the Cl further enhances the phase stability of the binary system $Cs_2SnI_xCl_{6-x}$ with an increased phase decomposition temperature. The new synthesis route and systematic investigation of the structural and optical properties and phase stability of $Cs_2SnI_xCl_{6-x}$ can provide new opportunities for optimizing the performance of Sn-based all inorganic perovskites.

Conflicts of interest

The authors declare no competing financial interests.

Acknowledgements

The synthesis of the perovskite for iodine and chlorine incorporation and environmental stability were supported as a part of the Center for Performance and Design of Nuclear Waste Forms and Containers, an Energy Frontier Research Center funded by the U.S. Department of Energy, Office of Science, Basic Energy Sciences under award # DE-SC0016584. Synchrotron X-ray diffraction was performed using Beamline 17-BM of the Advanced Photon Source (APS), a US DOE Office of Science User Facility operated for the DOE Office of Science by Argonne National Laboratory under contract no. DE-AC02-06CH11357. Y. Wang and J. Shi were supported by the National Science Foundation under Awards #1706815 and #1635520.

References

1 W. S. Yang, J. H. Noh, N. J. Jeon, Y. C. Kim, S. Ryu, J. Seo and S. I. Seok, *Science*, 2015, **348**(6240), 1234–1237.
2 M. M. Lee, J. Teuscher, T. Miyasaka, T. N. Murakami and H. J. Snaith, *Science*, 2012, **338**(6107), 643–647.
3 M. A. Green, A. Ho-Baillie and H. J. Snaith, *Nat. Photonics*, 2014, **8**(7), 506–514.
4 M. Grätzel, *Nat. Mater.*, 2014, **13**(9), 838.
5 M. H. Kumar, S. Dharani, W. L. Leong, P. P. Boix, R. R. Prabhakar, T. Baikie, C. Shi, H. Ding, R. Ramesh, M. Asta, M. Graetzel, S. G. Mhaisalkar and N. Mathews, *Adv. Mater.*, 2014, **26**(41), 7122–7127.
6 C. C. Stoumpos, C. D. Malliakas and M. G. Kanatzidis, *Inorg. Chem.*, 2013, **52**(15), 9019–9038.
7 T. Krishnamoorthy, H. Ding, C. Yan, W. L. Leong, T. Baikie, Z. Zhang, M. Sherburne, S. Li, M. Asta, N. Mathews and S. G. Mhaisalkar, *J. Mater. Chem. A*, 2015, **3**(47), 23829–23832.
8 B. W. Park, B. Philippe, X. Zhang, H. Rensmo, G. Boschloo and E. M. Johansson, *Adv. Mater.*, 2015, **27**(43), 6806–6813.
9 B. Saparov, F. Hong, J.-P. Sun, H.-S. Duan, W. Meng, S. Cameron, I. G. Hill, Y. Yan and D. B. Mitzi, *Chem. Mater.*, 2015, **27**(16), 5622–5632.
10 F. Hao, C. C. Stoumpos, D. H. Cao, R. P. Chang and M. G. Kanatzidis, *Nat. Photonics*, 2014, **8**(6), 489–494.
11 X. Qiu, Y. Jiang, H. Zhang, Z. Qiu, S. Yuan, P. Wang and B. Cao, *Phys. Status Solidi RRL*, 2016, **10**(8), 587–591.
12 B. Lee, A. Krenselewski, S. I. Baik, D. N. Seidman and R. P. Chang, *Sustainable Energy Fuels*, 2017, **1**(4), 710–724.
13 R. G. Niemann, A. G. Kontos, D. Palles, E. I. Kamitsos, A. Kaltzoglou, F. Brivio, P. Falaras and P. J. Cameron, *J. Phys. Chem. C*, 2016, **120**(5), 2509–2519.
14 J. H. Noh, S. H. Im, J. H. Heo, T. N. Mandal and S. I. Seok, *Nano Lett.*, 2013, **13**(4), 1764–1769.
15 P. Docampo, F. C. Hanusch, S. D. Stranks, M. Döblinger, J. M. Feckl, M. Ehrensperger, N. K. Minar, M. B. Johnston, H. J. Snaith and T. Bein, *Adv. Energy Mater.*, 2014, **4**, 1400355.

16 Q. Chen, H. Zhou, Y. Fang, A. Z. Stieg, T.-B. Song, H.-H. Wang, X. Xu, Y. Liu, S. Lu, J. You, P. Sun, J. Mckay, M. S. Goorsky and Y. Yang, *Nat. Commun.*, 2015, **6**, 7269.
17 A. Albinati and B. Willis, *J. Appl. Crystallogr.*, 1982, **15**(4), 361–374.
18 B. H. Toby and R. B. Von Dreele, *J. Appl. Crystallogr.*, 2013, **46**(2), 544–549.
19 K. Momma and F. Izumi, *J. Appl. Crystallogr.*, 2008, **41**(3), 653–658.
20 S. Park, W. J. Chang, C. W. Lee, S. Park, H.-Y. Ahn and K. T. Nam, *Nat. Energy*, 2016, **2**, 16185.
21 S. Colella, E. Mosconi, P. Fedeli, A. Listorti, F. Gazza, F. Orlandi, P. Ferro, T. Besagni, A. Rizzo, G. Calestani, G. Gigli, F. D. Angelis and R. Mosca, *Chem. Mater.*, 2013, **25**(22), 4613–4618.
22 M. I. Dar, N. Arora, P. Gao, S. Ahmad, M. Grätzel and M. K. Nazeeruddin, *Nano Lett.*, 2014, **14**(12), 6991–6996.
23 S. T. Williams, F. Zuo, C.-C. Chueh, C.-Y. Liao, P.-W. Liang and A. K.-Y. Jen, *ACS Nano*, 2014, **8**(10), 10640–10654.
24 L. Vegard, *Z. Phys.*, 1921, **5**(1), 17–26.
25 R. D. Shannon, *Acta Crystallogr., Sect. A: Cryst. Phys., Diffr., Theor. Gen. Crystallogr.*, 1976, **32**(5), 751–767.
26 J. Chae, Q. Dong, J. Huang and A. Centrone, *Nano Lett.*, 2015, **15**(12), 8114–8121.
27 S. Dastidar, D. A. Egger, L. Z. Tan, S. B. Cromer, A. D. Dillon, S. Liu, L. Kronik, A. M. Rappe and A. T. Fafarman, *Nano Lett.*, 2016, **16**(6), 3563–3570.
28 D. Sabba, H. K. Mulmudi, R. R. Prabhakar, T. Krishnamoorthy, T. Baikie, P. P. Boix, S. Mhaisalkar and N. Mathews, *J. Phys. Chem. C*, 2015, **119**(4), 1763–1767.
29 B. Lee, C. C. Stoumpos, N. Zhou, F. Hao, C. Malliakas, C.-Y. Yeh, T. J. Marks, M. G. Kanatzidis and R. P. Chang, *J. Am. Chem. Soc.*, 2014, **136**(43), 15379–15385.
30 P. Gao, M. Grätzel and M. K. Nazeeruddin, *Energy Environ. Sci.*, 2014, **7**(8), 2448–2463.
31 B.-w. Park, S. M. Jain, X. Zhang, A. Hagfeldt, G. Boschloo and T. Edvinsson, *ACS Nano*, 2015, **9**(2), 2088–2101.
32 Z. Zhang, B. Men, Y. Liu, H. Gao and Y. Mao, *Nanoscale Res. Lett.*, 2017, **12**(1), 84.
33 F. Guo, Z. Lu, D. Mohanty, T. Wang, I. B. Bhat, S. Zhang, S. Shi, M. A. Washington, G.-C. Wang and T.-M. Lu, *Mater. Res. Lett.*, 2017, **5**(8), 540–546.
34 B. Saparov, J.-P. Sun, W. Meng, Z. Xiao, H.-S. Duan, O. Gunawan, D. Shin, I. G. Hill, Y. Yan and D. B. Mitzi, *Chem. Mater.*, 2016, **28**(7), 2315–2322.
35 T. Briggs, *J. Phys. Chem.*, 1930, **34**(10), 2260–2266.

